

PAPER

Characterization of disruption mitigation via massive gas injection on MAST

To cite this article: A J Thornton *et al* 2012 *Plasma Phys. Control. Fusion* **54** 125007

View the [article online](#) for updates and enhancements.

Related content

- [Plasma profile evolution during disruption mitigation via massive gas injection on MAST](#)
A.J. Thornton, K.J. Gibson, I.T. Chapman *et al.*
- [Disruption mitigation by massive gas injection in JET](#)
M. Lehnen, A. Alonso, G. Arnoux *et al.*
- [Assimilation of impurities during massive gas injection in ASDEX Upgrade](#)
G. Pautasso, A. Mlynek, M. Bernert *et al.*

Recent citations

- [Disruption mitigation with high-pressure helium gas injection on EAST tokamak](#)
D.L. Chen *et al*
- [Thermal quench mitigation and current quench control by injection of mixed species shattered pellets in DIII-D](#)
D. Shiraki *et al*
- [Mitigation of upward and downward vertical displacement event heat loads with upper or lower massive gas injection in DIII-D](#)
E. M. Hollmann *et al*



IOP | ebooks™

Bringing you innovative digital publishing with leading voices to create your essential collection of books in STEM research.

Start exploring the collection - download the first chapter of every title for free.

Characterization of disruption mitigation via massive gas injection on MAST

A J Thornton¹, K J Gibson², J R Harrison¹, M Lehnen³, R Martin¹,
A Kirk¹ and the MAST Team

¹ EURATOM/CCFE Fusion Association, Culham Science Centre, Abingdon, Oxon, OX14 3DB, UK

² York Plasma Institute, Department of Physics, University of York, Church Lane, Heslington, York, YO10 5DD, UK

³ Institute for Energy Research - Plasma Physics, Association EURATOM/FZJ, D-52425, Jülich, Germany

E-mail: andrew.thornton@ccfe.ac.uk

Received 13 July 2012, in final form 22 October 2012

Published 12 November 2012

Online at stacks.iop.org/PPCF/54/125007

Abstract

Disruptions are of significant concern to future devices, due to the large amount of energy released during the rapid quenching of the plasma. Disruption mitigation has been performed on MAST, to study the effect on heat loads and disruption time scales in a spherical tokamak. Massive gas injection is performed using a disruption mitigation valve capable of injecting between 0.6 and 1.5×10^{22} particles, corresponding to 10–150 times the plasma inventory. Noble gases are used for mitigation studies, specifically helium, argon, neon and a mixture of 10% argon and helium. The effect of mitigation is studied using a comparison between mitigated discharges and reference unmitigated disruptions.

Mitigation has been seen to be effective at reducing peak divertor power loads, with reductions of up to 60% in the divertor power load being observed. The decrease in divertor power load is reflected by an increase in radiated power, mainly as a result of line radiation from the injected impurities. The largest reduction in the divertor power loads are seen for the impurities with $Z > 4$. The energy load to the divertor has been reduced by between 30–40% of the total stored plasma energy in ohmic, L mode and H mode discharges. Mitigation also affects the current quench times, accelerating the quench of the plasma with increasing injection quantity, with saturation observed at the highest injected quantities.

(Some figures may appear in colour only in the online journal)

1. Introduction

Disruptions pose a significant risk to future devices due to the large heat fluxes and vessel forces which are generated [1]. In present day machines, the disruption heat fluxes and stresses can generally be tolerated. However, the order of magnitude increase in stored energy in future devices requires that steps to mitigate the deleterious effects of a disruption must be employed. An unmitigated disruption typically shows two distinct phases. The first phase is the thermal quench, which is the period when the stored thermal energy in the plasma is lost [2]. This is the phase in which the largest divertor heat loads are generated [3]. The rapid cooling during the thermal quench phase leads to an increased plasma resistance,

subsequently leading to the current quench phase. The current quench phase corresponds to the loss of the stored magnetic energy, which is converted to thermal energy via ohmic heating of the post thermal quench plasma [4]. The rapid drop in plasma current during the current quench phase can induce currents in the vacuum vessel, leading to structural stresses. In elongated or shaped plasmas, the control of the vertical position of the plasma can be lost during the current quench phase. The subsequent vertical displacement event (VDE) brings the plasma into contact with the vessel, which causes current to flow in the vacuum vessel. These currents are known as halo currents and can generate large forces on the vessel as a result of interaction with the toroidal magnetic field. Finally, the sudden decay in plasma current generates large electric fields which

can accelerate electrons in the plasma to relativistic velocities. The relativistic electrons are known as runaway electrons and can generate significant localized heat fluxes when they interact with the vacuum vessel [5].

Various methods of disruption mitigation are available, principally killer pellet injection [6] and massive gas injection (MGI) [7]. Investigation of disruption mitigation via MGI has been performed in various tokamaks, including JET [8], ASDEX-Upgrade [9], TEXTOR [10], DIII-D [11], C-Mod [12] and Tore Supra [13]. MGI involves the injection of neutral impurity gases, typically noble gases, into the vacuum vessel. The quantity of injected gas is typically an order of magnitude above that in the plasma inventory. Studies have shown that MGI produces a controlled termination of the plasma, by radiating away the majority of the stored energy in the plasma via impurity line radiation [14].

MGI can also be used to control the current quench phase. The injection of impurities cools the plasma more rapidly compared to an unmitigated disruption, which decreases the plasma current at the time of the VDE. The increased speed of the current quench is advantageous in elongated plasmas, which typically exhibit a greater degree of vertical instability compared to circular plasmas [1]. The increased speed of the current quench which results from mitigation acts to minimize the duration of the VDE, thereby reducing the size of the halo currents generated [9]. The rapid current quench in unmitigated disruptions can lead to the formation of runaway electrons. One adverse consequence of the rapid speed of the current quench, which results from mitigation, is that there will be an increased likelihood and magnitude of runaway electron formation. However, the injection of a large quantity of impurity species into the plasma increases the density of the post thermal quench plasma compared to an unmitigated disruption. The increased density at the start of the current quench can act to collisionally suppress the runaway electrons [15].

Previous studies have been performed to study the mixing and evolution of the impurities into the plasma during MGI mitigated disruptions [14, 16, 17]. The focus of this paper is to study the effects of disruption mitigation in terms of heat loads, timescales and halo currents. Section 2 presents a brief overview of the MAST disruption mitigation valve (DMV) and the diagnostics used to study disruptions in MAST. Section 3 provides details of the various timescales and phases of a mitigated disruption which will be referred to throughout the rest of the paper. Section 4 details the discharges used to compare the effects of disruption mitigation. Section 5 outlines the timescales involved in the propagation of the injected impurities into the plasma edge, thereby defining a response time for the mitigation. Section 6 details the heat load analysis during the thermal quench, including assessment of the energy balance during the disruption for a range of mitigated plasmas, injected quantities and species. Section 7 describes the mitigation of the current quench forces, via current quench timescales and halo current magnitudes, with section 8 concluding the paper.

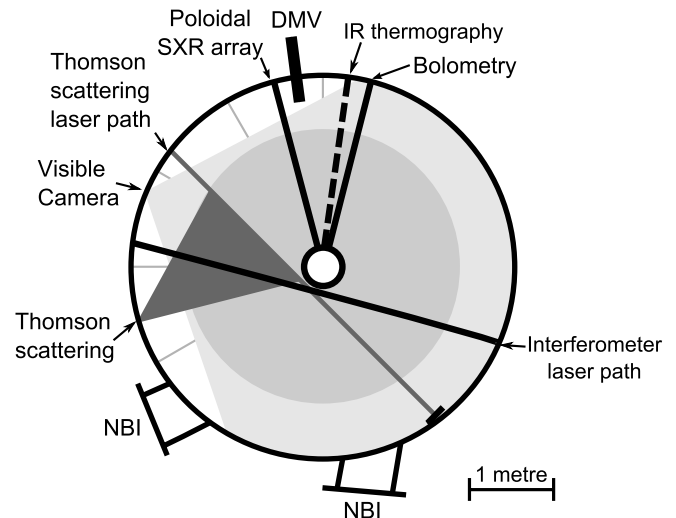


Figure 1. A top down view of the MAST vessel showing the location of the main diagnostics used to characterize disruptions. The location of the DMV is also shown. The plasma current direction and toroidal field direction in MAST are in the anticlockwise direction on the figure.

2. Disruption mitigation on MAST

Disruption mitigation on MAST [18] is performed using an eddy current actuated valve, which is capable of injecting up to 150 times the plasma inventory in 1–2 ms. The MAST DMV and valve operation have been described in detail in [16, 19].

A range of diagnostics are used to characterize disruptions on MAST. A comprehensive review of the diagnostics used for disruption mitigation is presented in [16], however, a brief outline is repeated here for convenience. The key diagnostics used for the studies reported here are shown in figure 1, which shows the location of the diagnostics relative to the injection location of the DMV. The measurement of the heat flux to the divertor are made using infrared thermography, which is able to view all of the four strike points in MAST during the discharge.

The radiated power from the plasma is determined using a gold foil bolometer located in the toroidal sector next to the DMV. The bolometer temporal resolution is approximately 0.4 ms, however, the response time of the gold foil detector and the smoothing required for analysis of the radiated power prevents time resolved radiated power measurements during the thermal and current quenches. Nevertheless, the bolometer response is sufficient to allow overall energy balance to be performed during both unmitigated and mitigated disruptions.

The number of particles injected during the mitigation of a discharge is determined using measurements of the DMV injection pressure before and after the firing of the DMV. The change in pressure and the DMV plenum volume (65 ml) is used to calculate the total number of particles injected into the vessel over the period of the plasma decay. Measurements of the pressure in the MAST vacuum vessel (volume 50 m³) using fast ion gauges have been used to calibrate the injected quantity of particles.

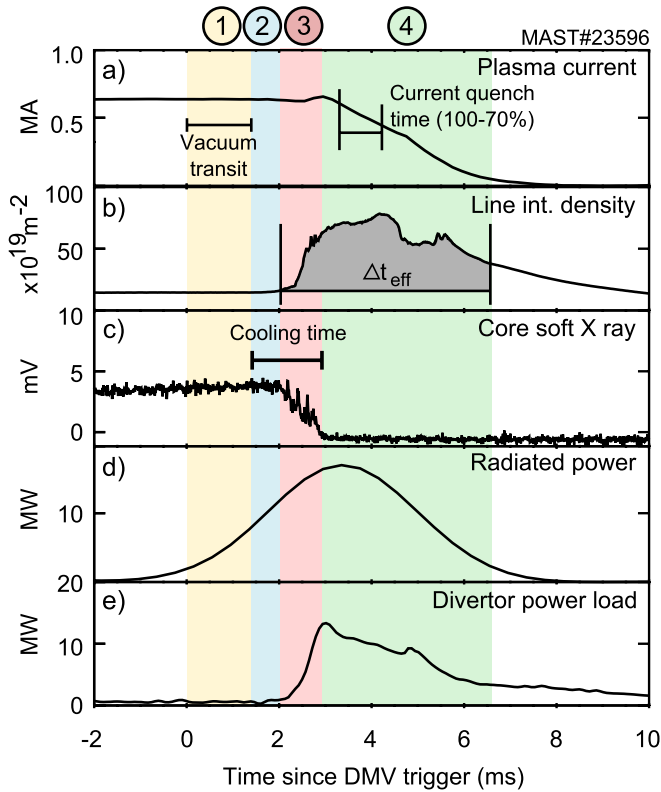


Figure 2. Characteristic timescales and phases of a mitigated disruption. The four phases, vacuum transit, edge cooling, thermal quench and current quench are shown, along with key time scales during the mitigation. The time over which the fuelling efficiency is calculated (Δt_{eff}) is shown, along with the region over which the density is integrated.

3. Disruption characteristics

Mitigated disruptions undergo several different phases and can be characterized by various timescales [8, 20, 21]. The phases of a mitigated discharge are shown in figure 2 which shows the evolution of the plasma in time, relative to the time of the DMV trigger. The first phase is the vacuum transit phase, where the gas propagates from the valve to the plasma. The time between the triggering of the DMV to the arrival of the gas at the plasma edge is defined as the vacuum transit time. The time of arrival of the gas at the plasma edge is determined using high speed (50 kHz) imaging. Upon arrival at the plasma edge, the cooling phase begins. The time between the arrival of the gas and the thermal quench of the plasma is defined as the cooling time. The cooling is brought about by line radiation from the injected impurities, as can be seen by the rise in the radiated power during this phase (d). The increase in the radiated power prior to the injection of the impurities is due to the slow temporal response of the bolometer, as discussed in section 2. The third phase of the mitigation is the thermal quench phase, where the stored energy from the plasma is lost to the divertor. The final phase is the current quench phase, where the current decays from the increased plasma resistivity as a result of the thermal quench cooling the plasma. The current quench phase is the period in which halo currents and induced currents are generated in the vessel.

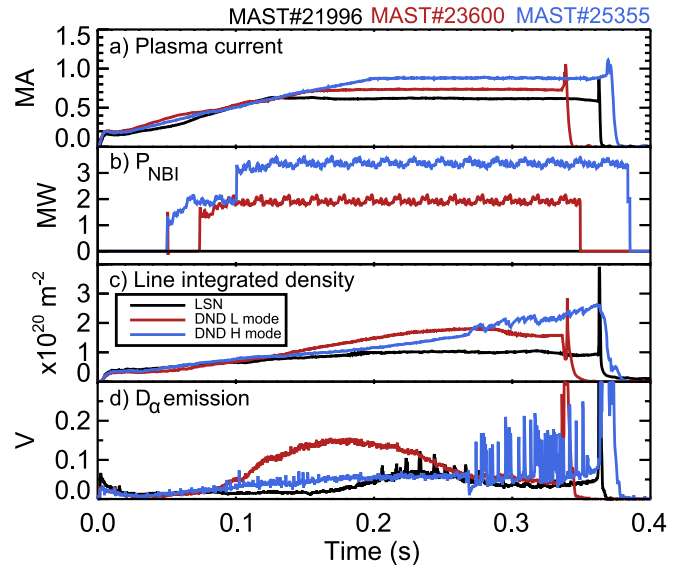


Figure 3. Typical plasma parameters of the discharges used for mitigation. The black trace shows an ohmic LSN reference discharge. The red trace shows a double null L mode discharge and the blue trace shows a double null H mode discharge which are both used as unmitigated reference disruptions.

4. Investigating the effect of mitigation on disruptions

The effect of disruption mitigation on a plasma can be investigated using two techniques. The first method involves directly comparing a discharge which is unmitigated to one which is mitigated. To achieve such a comparison, a discharge is taken which terminates disruptively, this discharge is then mitigated prior to the natural disruption and then the characteristics of the two disruptions can be compared. The reference disruption for these studies disrupts due to the presence of a $m/n = 1/1$ mode which grows during the plasma and eventually leads to thermal collapse of the plasma.

The second method involves mitigation of a single discharge, into which a range of different impurity species and quantity are injected. The data collected can then be used to optimize the performance of the mitigation. Comparison between these discharges and unmitigated discharges can be made by using disruptive discharges with similar plasma parameters. Both of these methods have been used to characterize disruption mitigation in MAST using two different target plasmas. In this paper, a comparison between a mitigated and unmitigated disruption is performed using a double null 750 kA beam heated L mode discharge and a 900 kA beam heated H mode plasma. The optimization of the MGI uses an ohmic 600 kA lower single null (LSN) discharge. Typical plasma parameters of the target discharges are shown in figure 3. The plasma parameters for the mitigated/unmitigated comparison for both the L mode and H mode discharges are shown in red and blue respectively. The plasma parameters of the discharge used to optimize the mitigation are shown by the black trace on figure 3.

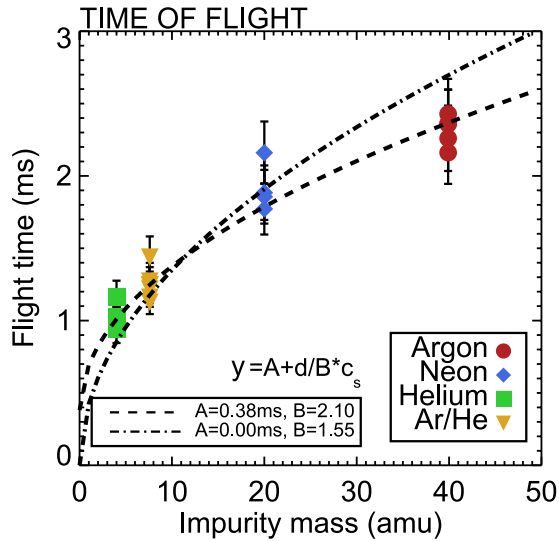


Figure 4. The vacuum transit time can be determined for a range of injection species. The data are fitted to the form $y = A + (d/Bc_s)$, where d is the distance to the plasma edge from the valve and c_s is the sound speed of the impurity.

5. Vacuum transit phase

The speed of propagation from the valve to the plasma edge is determined by the sound speed, c_s , of the impurity species used. The free expansion of gas into a vacuum is expected to occur at $3c_s$ [22]. The vacuum transit time is the time taken for the gas to travel from the valve to the plasma edge. The distance the gas must travel to the plasma edge varies based on the plasma configuration, but is typically of the order 1.8 m. Figure 4 shows the vacuum transit time as a function of impurity mass, the data are fitted to the form $y = A + (d/Bc_s)$, where d is the distance to the plasma edge from the valve and c_s is the sound speed of the impurity.

Figure 4 shows that the propagation speed of the impurities exceeds the sound speed of the impurities. The fitted data show that the impurities travel at $2.1c_s$ if a constant offset of 0.38 ms is applied to the fit. The flight time is determined using the valve trigger time and the arrival of the gas at the edge of the plasma. The time taken for the valve to open from the trigger being sent is not accounted for, therefore this is a possible source for the timing error. The opening time of the valve has previously been measured [19, 23] to be of the order 0.3–0.5 ms, which is consistent with the offset seen in the data shown in figure 4. The propagation speed is lower than the $3c_s$ expected from free expansion, however, the results are consistent with data from other tokamaks, which measure propagation at $2.5c_s$ [8], and from laboratory testing [24]. The slowing of the vacuum transit time compared to the theoretical time may be due to the drag which is imparted on the gas flow by the walls of the pipe as the gas travels from the valve to the plasma edge [24].

5.1. Plasma cooling times

The arrival of the impurities at the plasma edge leads to line radiation which acts to dissipate the stored thermal energy in

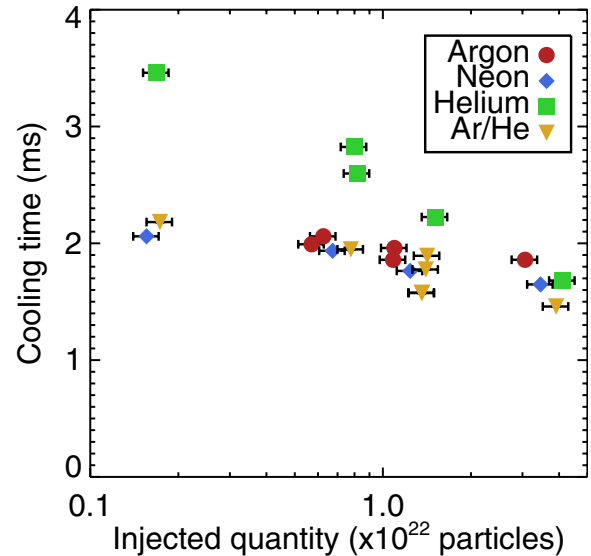


Figure 5. Cooling time as a function of the injected species and quantity. The cooling time is defined as the period between the gas arriving at the plasma edge and the time of the current spike.

the plasma. The cooling time is defined as the time between the arrival of the gas at the plasma edge and the current during the current spike, as shown in figure 2. The definition of the cooling time used here is the same as that used in [8, 13], however, some other studies do not include the thermal quench time in the definition of the cooling time, such as [15]. Figure 5 shows the cooling time plotted as a function of injected quantity and species. Figure 5 shows that the cooling time decreases when impurities with $Z > 4$ are used. There is also a weak dependence of the cooling time on injected quantity, with increased injection levels increasing the speed of the cooling. The dependence of the cooling time on the injected quantity and species is expected, as the varying these quantities leads to increased radiative loss from the plasma either by increased radiative loss per ion or by increasing the total number of radiators. The increased radiation with increasing impurity mass leads to more rapid cooling and a faster quench time.

The increased impurity assimilation during the cooling phase can be seen in figure 6. The largest density rises are seen for low mass impurities, such as helium and Ar/He mixtures with the smallest density rise for pure argon. The higher sound speed of helium permits a larger number of particles to be delivered to the plasma edge prior to the thermal quench. The delay between the arrival of the impurities at the plasma edge and the time of the peak density is seen to depend on impurity mass, with higher mass gases exhibiting a longer delay. These observations are consistent with the increased propagation time for the higher mass gases from the DMV injection location to the interferometer viewing chord. It is thought that the level of impurity assimilation is determined by the quantity of impurities delivered to the plasma edge prior to the thermal quench [25]. Therefore, light mass species lead to larger density rises than low mass species. The long cooling time for helium compared to neon and argon suggest that the dominant factor is the radiative loss per ion, rather than the total number of radiating ions present. This observation is

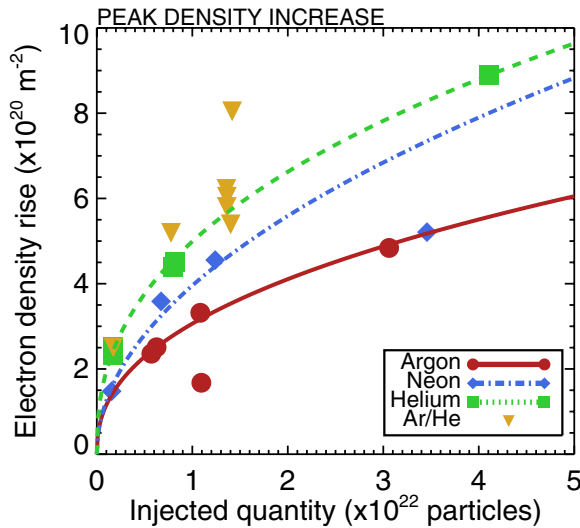


Figure 6. Peak electron density rise during the mitigation as a function of injected quantity and species, as measured using interferometry.

also supported by the limited dependence of the cooling time on increased injection quantity.

6. Thermal quench phase

In a disruption, the thermal quench phase marks the point where the stored thermal energy in the plasma is lost to the divertor surfaces. In mitigated disruptions, some of the thermal energy has been radiated away prior to the onset of the thermal quench where the remainder is lost. The loss of energy leads to the divertor heat flux rising rapidly as the stored energy is transmitted from the plasma to the divertor [1]. The heat fluxes to the divertor can be monitored in MAST using infrared (IR) thermography [26], allowing an assessment of the heat flux to be made. MAST is a graphite walled machine with a distant wall, therefore it is not expected that there will be a significant contribution from reflection of IR radiation onto the divertor surfaces on the heat fluxes measured. The determination of the divertor heat flux is performed by solving the heat flux equation [27] including the effect of surface layers [28] which are used to account for hydrocarbon layers and surface irregularities in MAST [26, 29]. In order to determine the surface layer coefficients for the divertor surfaces, comparison is made between Langmuir probe measurements and the IR. In addition, a coefficient is selected which removes the negatives in the IR profiles. The chosen surface layer coefficient is then used to perform energy balance during unmitigated disruptions, where good agreement is seen confirming the choice of coefficient.

The open nature of MAST [30] allows the divertor surfaces to be imaged directly, without the need to view the divertor through the plasma. The direct imaging of the divertor minimizes the effect of impurity line radiation, generated via MGI, on the measured divertor temperatures [31]. The effect of background emission on the IR measurements can be assessed by imaging areas of the divertor where no heat flux should fall. The IR thermography on MAST images a section of the

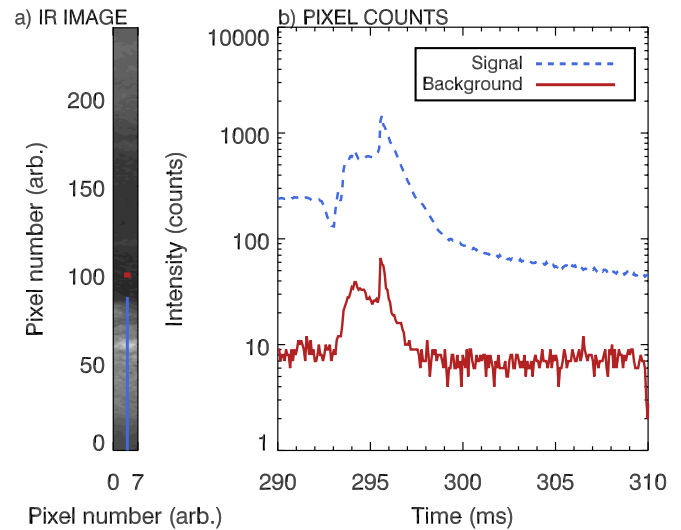


Figure 7. The effect of background emission on the IR photon counts during mitigation. The peak counts along the analysis lines shown in (a) is plotted as a function of time in (b). The dashed line is an analysis path in the region where the heat flux falls and the solid line is the analysis path in the shadowed region. The valve is triggered at 290 ms, with the thermal quench following at 293 ms. The analysis lines cover the outer divertor region, where the heat flux falls and the shadowed region of the divertor under the divertor coil armour.

inner divertor, coil armour around the divertor coil and the outer divertor. The region beneath the divertor coil armour is shadowed from heat flux. Imaging the shadowed region provides a means of quantifying the background level of IR emission during mitigation. A sample frame from the IR thermography system is shown in figure 7(a), along with two analysis paths along which the camera counts are measured, one region covers the outer divertor and the other region is in the shadowed region. The camera counts along these paths are plotted around the disruption time in figure 7(b). The data shown in figure 7 show that the signal in the shadowed region (solid line) is insignificant compared to the counts in the region where the heat flux is deposited onto the divertor (dashed line). The data shown in figure 7 are from a long wave (7.6–9.0 μm) IR camera, and shows that the background level amounts to 7% of the signal from the divertor heat load at the time of the peak divertor heat load. Similar measurements performed on the medium wave (4.5–5.0 μm) camera, show that the background signal level is lower, constituting 1% of the counts in the outer divertor region at peak heat flux. The error induced from background plasma emission during mitigation is well within the normal error of the IR data of ± 10 –20%, and so this does not play a significant role.

6.1. Divertor power loads

The power to the divertor strike points can be measured during a mitigated and an unmitigated disruption. The deposited power at all of the four strike points is shown in figure 8. During steady state plasmas, the power load to the outer strike point (OSP) is of the order 10 times larger than the inner power load [32]. The in/out balance also favours the outer divertor during the disruptive phase as seen in figure 8.

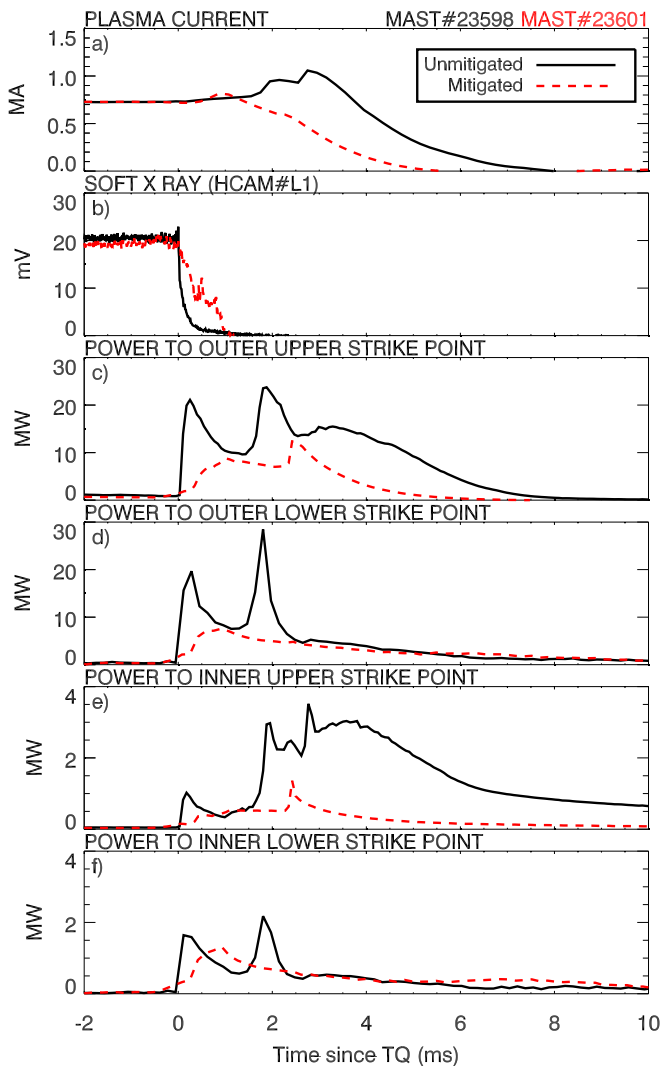


Figure 8. Divertor power load during an unmitigated and a mitigated disruption. The time axis is normalized to the thermal quench, which is defined as the first drop in the core soft x ray emission (see (b)). The extended SXR emission after the initial decrease is caused by the increase in density seen during the mitigation, and is not representative of an increase in the thermal quench duration due to mitigation. The power load to each of the four strike points is shown.

The evolution of the power load in the unmitigated case starts with a sudden rise in the power load which is associated with a fall in the soft x ray emission figure 8(b). Analysis of high speed camera images and Mirnov coil data during this time show that the unmitigated disruption is initiated by the growth of a large plasma mode which leads to the ejection of a filament of plasma at the time of the first rise in the divertor power load. The ejection of the filament marks the onset of the thermal quench of the plasma, with the core plasma temperature falling from 1 keV to 150 eV after the interaction of the filament with the divertor and surrounding coil structures. The plasma survives this initial quench, with a second thermal quench occurring 1.5 ms after the first heat pulse to the divertor. The second thermal quench deposits the remaining stored thermal energy onto the divertor, as seen by the increase in the divertor power load 2 ms after the onset

of the thermal quench in figure 8. Throughout the thermal quench phase, the power load to the upper and lower divertors are comparable, suggesting that there is little vertical motion of the plasma during this phase, and that the plasma remains as a connected double null plasma.

Following the thermal collapse of the plasma, the power load is maintained by the dissipation of the stored magnetic energy from the plasma during the current quench phase [4]. In the phase of the disruption from 2.5 ms after the thermal quench, the power load to the upper divertor exceeds that to the lower divertor, which is consistent with the vertical motion of the plasma seen via high speed imaging during this period.

The mitigated case shown in figure 8 shows a significant overall reduction in the power load to the divertor compared to the unmitigated case. The power load to the divertor at the onset of the mitigated thermal quench rises over a one millisecond time period, consistent with the rate of fall of the soft x ray emission. Once the soft x ray emission has fallen to zero, indicating that the thermal energy has been lost, the power load begins to decay as the magnetic energy is dissipated from the plasma. The power load decays smoothly from this point on the lower divertor. The upper divertor power load also decays after the thermal energy is exhausted, however, an increase in power is observed 2.5 ms after the onset of the thermal quench. The increase in the power load at this time is consistent with the interaction of the plasma with the upper divertor as a result of a loss of vertical control as seen via high speed imaging of the plasma. Further assessment of the vertical motion of the plasma during the current quench stage will be made in section 7.2 when the mitigation of halo current is discussed. The total duration of the disruption power load decreases from 8 to 6 ms using mitigation, and the peak power load falls by 60%.

Mitigation using different impurity species and quantity has been investigated on MAST and has been shown to affect the reduction in power load during the mitigation. The species and injected quantity effect can be studied using repeated mitigations into the same target discharge. Figure 9 shows the outer strike point (OSP) heat flux as a function of injected quantity and for a range of different impurity species. The range of injected quantity is varied between 0.6×10^{22} and 4.0×10^{22} particles. The peak divertor heat flux is independent of the injected quantity over the range investigated. The lowest reduction in peak heat flux occurs for helium injection. Increasing the impurity species mass is seen to have no significant effect on decreasing the heat flux to the target further, with both argon and neon injection leading to peak values of the order of 20–30 MW.

6.2. Radiated power

The radiation produced by the injected impurities interacting with the plasma dissipates the stored energy contained within the plasma [20]. The radiation levels can be monitored using a gold foil bolometer as detailed in section 2. To determine the radiated energy, the radiated power recorded from the bolometer is integrated in time, and toroidal symmetry is assumed in the radiated power measurement.

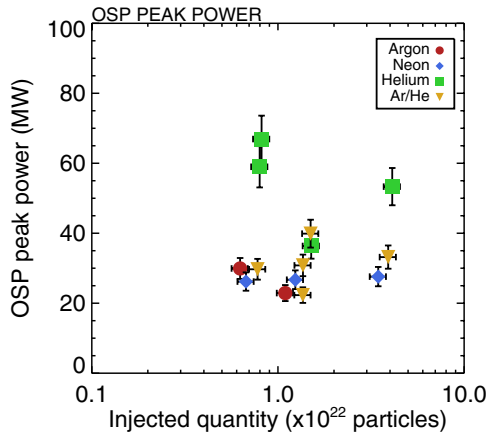


Figure 9. Peak divertor heat flux to the outer strike point as a function of injected species and quantity.

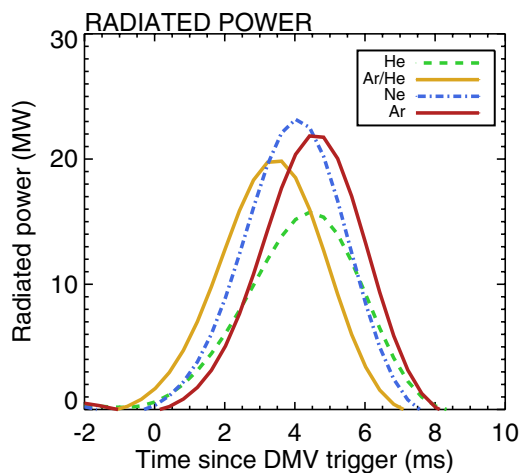


Figure 10. Radiated power during the disruption as a function of time and impurity species. The injection pressure is fixed at 5 bar.

The radiated power during the mitigation for a range of impurity species is shown in figure 10, using an injection pressure of 5 bar. The radiated power data are consistent with the power load to the divertor in figure 9, where increased radiation gives rise to lower divertor power loadings. Whilst the DMV pressure is constant for the data in figure 10, variations in the sound speed of the gas cause the number of injected particles to vary by 20% between the argon and helium traces [19, 33]. The data show that the radiated power is the highest for argon and neon injection compared to pure helium injection. The levels for the argon and neon injection are similar to each other in magnitude. The radiated power is the lowest in helium, with the argon/helium mixture lying between these species.

6.3. Energy balance in ohmic discharges

The energy lost during a disruption can be determined from the sum of the radiated energy and the energy deposited onto the divertor. The total energy delivered to the divertor can be found by assuming the power load is toroidally symmetric and integrating the power load measured using the IR cameras over the time of the disruption. The radiated energy during

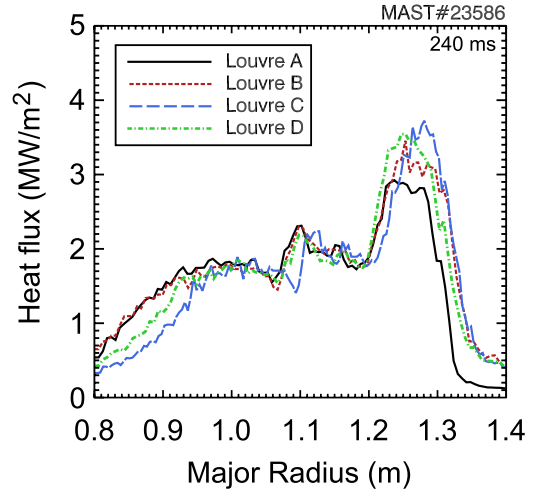


Figure 11. The heat flux to the divertor during a mitigated discharge showing the heat flux profiles across various divertor louvres displaced toroidally. The profiles are taken at the peak of the disruption heat load. In order to obtain a wide angle view, the IR camera is operated at a reduced frame rate of 800 Hz. The toroidal separation between two adjacent louvres is 30°. The IR camera coverage spans from 0.8 to 1.4 m in radius.

the disruption can be found from integration of the radiated power. The total energy lost from the plasma (divertor and radiated) can be compared to the total stored energy from the plasma. The total stored energy is determined using EFIT reconstruction [34] prior to the triggering of the DMV. Approximately 80% to 100% of the total stored energy in the plasma can be accounted for in both mitigated and unmitigated disruptions using these assumptions. The unaccounted energy is the largest in double null mitigated discharges and the lowest in LSN mitigated discharges. There are several possible sources for the unaccounted energy; firstly, the error on the EFIT stored energy can be of the order $\pm 10\%$ in typical MAST discharges. Further, the assumption of toroidal symmetry in the heat flux may not be accurate. However, analysis of wide angle IR thermography shown in figure 11, covering several toroidal angles of the divertor, has shown limited variation in the divertor heat loads. It can be seen in figure 11 that the heat flux footprint can fall outside the region covered by the infrared camera during the peak of the disruption heat flux. These effects, coupled with the deposition of the heat flux onto other unmonitored components, such as the centre column or poloidal field coils provide a source of error for the unaccounted energy. Further work, such as measurement of the heat load on invessel coils and the centre column will be required to quantify the exact magnitude and distribution of the energy loadings to these surfaces during disruptions.

The divertor energy load in mitigated discharges is shown in figure 12 for a range of discharge types, mitigation species and quantities. The largest reduction in the energy deposited onto the divertor occurs for the injection of the highest mass species. The divertor energy loads using helium mitigation are comparable to those seen without mitigation, where 80% of the total stored energy arrives at the divertor surfaces. Divertor energy load mitigation appears to be more effective in double null discharges (DNDs) compared to lower single

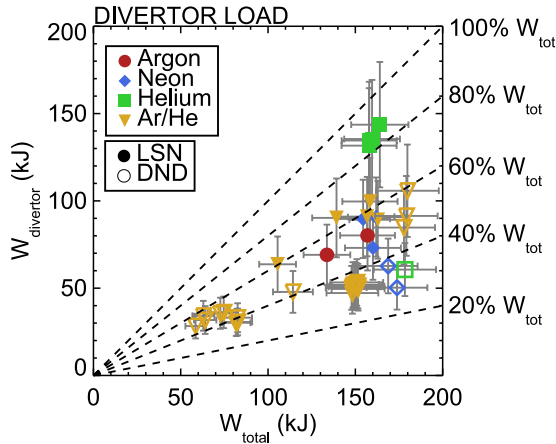


Figure 12. The fraction of energy deposited onto the divertor surface during mitigated ohmic plasmas in MAST. Mitigation is performed using a range of impurity species into both DND and LSN discharges.

null (LSN) discharges. The mitigation of the discharges using neon and argon give rise to similar levels of divertor energy load, suggesting that there is a limit to which the divertor energy load can be reduced, which reflects the peak divertor power load data shown in figure 9. The use of a mixture of helium and argon is also effective at reducing the divertor heat loads, giving similar reductions in divertor heat loads as pure argon. The effect of mitigation is to reduce the divertor energy load to 40% of the total stored energy in the ohmic discharges studied.

6.4. Energy balance during beam heated L and H mode plasmas

A range of double null plasmas have been mitigated using a 5 bar injection of an Ar(10%)/He mixture. The mitigated plasmas include those shown in figure 3, plus additional ohmic discharges to produce a scan in total stored plasma energy. The data in figure 13 show the energy deposited onto the divertor as a function of the stored thermal energy in these discharges. The range of stored energy spans from 50 to 300 kJ for the ohmic and neutral beam heated H modes respectively. The data shown in figure 13 show that mitigation reduces the energy arriving at the divertor to between 30% and 40% of the total stored energy in the plasma prior to mitigation for all of the stored energies investigated.

6.4.1. L mode beam heated discharges. A direct comparison of the energy balance in an unmitigated disruption and a mitigated disruption can be performed to determine the effect of mitigation on the balance between radiated energy and the energy carried to the divertor. The injection of the impurities leads to an increase in the vacuum vessel pressure, which affects the neutral beam injection (NBI) lines. In order to prevent damage to the NBI system as a result of ionisation of the beam from the increased vessel pressure, the beam injection is stopped 15 ms before the triggering of the valve. The 15 ms delay is set by hardware constraints on the control system of the NBI system and is significantly shorter than both the energy

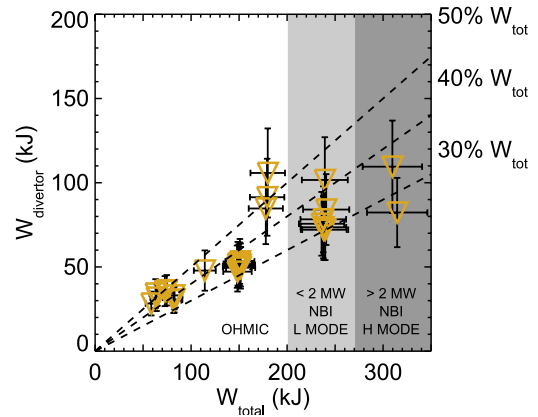


Figure 13. Energy arriving at the divertor as a function of the total stored plasma energy in DNDs. The mitigation of the plasma is performed using a 5 bar injection of an Ar(10%)/He mixture. The greyed regions represent discharges with NBI in both L mode and H mode.

confinement time of 30 ms and the beam slowing down time of 20–60 ms [35]. The effect of isolating the NBI early is to decrease the stored thermal energy at the time of the mitigation by 10–15% compared to the unmitigated reference. However, the stored magnetic energy (175 kJ) dominates over the thermal energy and this is comparable in both cases. The difference between the total stored energy at the time of the disruption in the mitigated and unmitigated cases is of the order 9%.

Mitigation of the plasma increases the fraction of radiated power. The power radiated from the plasma can also affect the power delivered to the divertor, as the power arriving at the divertor can be conducted from the plasma or delivered to the divertor by absorption of the radiated power. Estimation of the energy arriving at the divertor as a result of the radiation suggests that the heat flux on the divertor as a result of radiation only is 0.5 MW m^{-2} , compared to the heat flux during mitigation of approximately 6 MW m^{-2} . Integration of the estimated heat flux from radiation on the divertor over the exposed divertor area during the mitigation gives a total deposited energy of 2.5 kJ, which amounts to 6% of the energy measured at the divertor using the IR. The estimate of the radiated power load on the divertor assumes that the radiation is toroidally and poloidally uniform. Visible imaging [16, 21] suggests that the radiation is localized at the injection location, making the 6% an upper estimate on the divertor power load resulting from radiation.

The comparison between the unmitigated and mitigated disruption is shown in figure 14. Mitigation of the discharge reduces the divertor energy load by 52% with a corresponding increase in the radiated energy. The increase in the radiated energy is expected as a result of the injection of impurities into the plasma. The unmitigated disruption shows that the radiated energy is 10% of the total stored energy in the plasma, with 70% reaching the divertor. Analysis of a range of unmitigated MAST disruptions shows that these values are typical, with the divertor energy load being of the order 80% of the total energy on average.

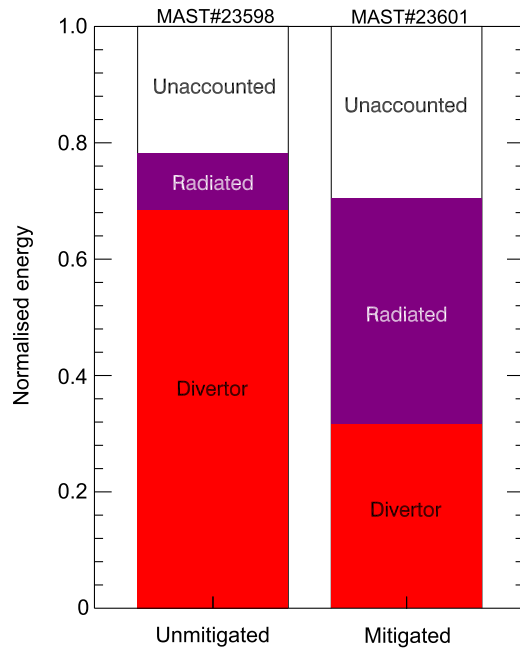


Figure 14. Comparison of the energy deposited during an unmitigated and mitigated disruption in a one beam L mode discharge. The radiated and divertor energy is normalized to the total stored energy (magnetic and thermal) in the plasma.

6.4.2. H mode beam heated discharges. Mitigation of an H mode plasma has been performed, with the reference plasma shown in blue in figure 3. As in the one beam case L mode case, the NBI ceases 15 ms before the triggering of the DMV at 360.9 ms. The termination of the beam heating can lead to the loss of the H mode prior to the arrival of the impurities at the plasma edge. Repeated discharges have been performed and those which have transitioned out of H mode at the time of the onset of the mitigation have been removed from subsequent analysis.

The total stored energy at the time of mitigation in the H mode case is of the order 300 kJ, of which approximately 100 kJ is thermal energy contained in the plasma and 200 kJ is magnetic energy carried by the poloidal magnetic field. The peak core electron temperature reaches 1.3 keV in these discharges, with a core electron density of $6 \times 10^{19} \text{ m}^{-3}$. The pedestal temperature in the H mode case is 200 eV compared to the edge (Ψ_{95}) temperature in the L mode case of 60 eV.

The evolution of an H mode discharge is shown in figure 15 and follows the sequence seen in ohmic and L mode mitigation, with an additional phase resulting in the loss of the H mode. The injected impurities travel to the plasma edge, arriving 1.2 ms after the triggering of the DMV as determined using high speed visible imaging. The arrival can be seen as a decrease in the soft x-ray emission in figure 15(c). At the time the impurities arrive the plasma is in H mode, as shown by (b). The arrival of the impurities at the plasma edge give rise to cooling of the plasma and a transition from H to L mode. Measurements of the core electron temperature using Thomson scattering (TS) show that the central temperature falls from 1.3 to 0.7 keV after the HL transition. The transition from H to L mode deposits energy onto the divertor as measured by the IR camera ((e) and (f)). The cooling of the plasma

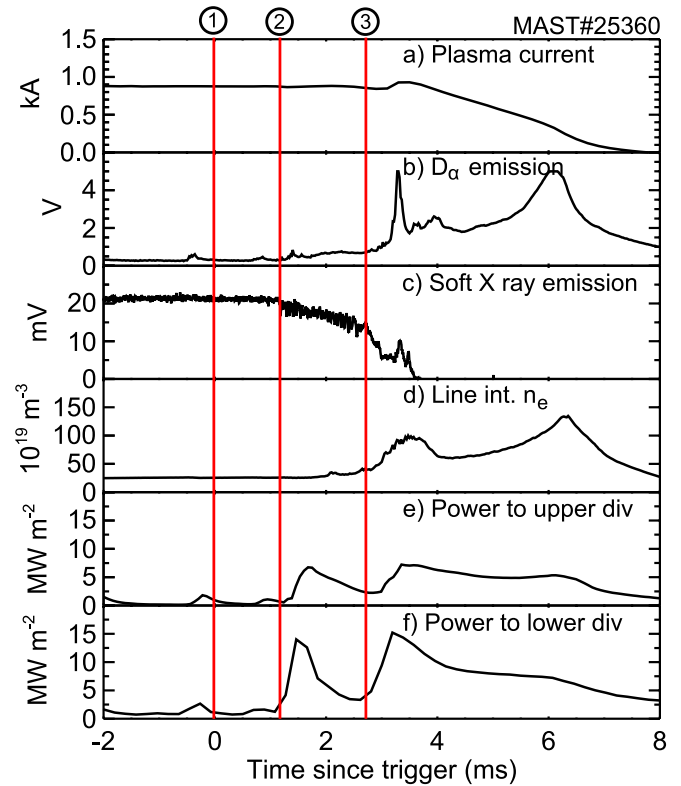


Figure 15. A typical H mode mitigation sequence, for injection of 5 bar of an Ar(10%)/He mixture. The times are normalized to the time of the DMV trigger which occurs at 360.9 ms as shown by the vertical line at 1. The arrival of the impurities at the edge of the plasma occurs 1.2 ms after the trigger, as shown by line 2. The arrival of the impurities is determined by fast imaging. The thermal quench occurs after the cooling period as shown by line 3.

continues with the thermal quench of the plasma, occurring 2.7 ms after the firing of the valve, marked by the sudden drop in the soft x ray emission, fall in the core electron temperature as measured by the TS system (not shown) and the subsequent rise in the divertor heat load after the initial heat pulse from the HL transition. The remaining stages of the mitigation proceed as described above and in [16]. The heat flux to the lower divertor is seen to be higher in this case compared to the beam heated L mode shown in figure 8 due to a lower plasma height in the case of the H mode plasma. The plasma is seen to be vertically stable throughout the mitigation sequence based on Mirnov coil measurements of the plasma position and supported by the absence of a sudden increase in the heat flux to the divertor during the current quench phase.

Comparison of the total energy contained within the H mode plasma prior to the disruption and the quantity radiated or deposited onto the divertor gives energy balance of between 60% and 75%. The discrepancy in the energy balance is larger in the H mode discharges and further work is required to reconcile the difference in the energy loss.

The energy deposited onto the divertor in the mitigated H mode is similar to the levels seen in the ohmic and L mode cases. The divertor energy fraction amounts to 37% of the total stored magnetic energy in the H mode plasma (figure 13), with a radiated energy fraction of 32%. A similar unmitigated disruption in a repeat discharge gives a divertor energy load of

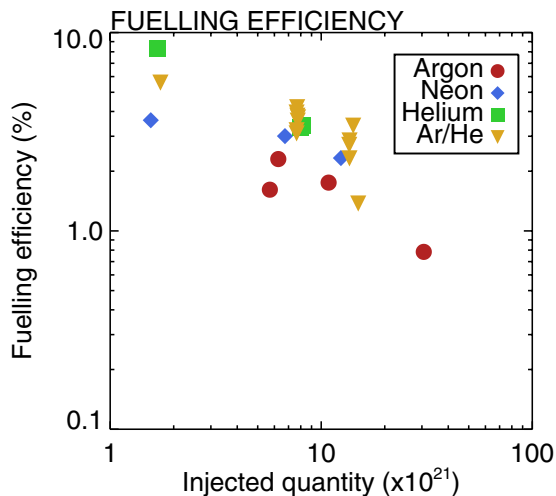


Figure 16. The fuelling efficiency as a function of the injected quantity and species. The fuelling efficiency is determined using the average density rise during the mitigation as measured using a CO₂ interferometer.

72% of the total stored plasma energy and a radiated fraction of 5%. There is a consistent fall in the divertor energy with the rise in the radiated fraction between the mitigated and unmitigated disruptions, within the error possible on the measurements (of the order 10–20%).

6.5. Fuelling efficiency during mitigation

The fraction of impurities entering the plasma can be determined using the electron density rise during the mitigation. The electron density can be measured using a Michelson CO₂ interferometer throughout the mitigation of the plasma. The location and laser path of the interferometer is shown in figure 1. The fuelling efficiency is defined as the electron density rise for a given number of injected impurities. The determination of the fuelling efficiency is made using the approach used by ASDEX-Upgrade [15], where the density increase is integrated between the thermal quench time and the time at which the plasma current reaches 20% of the pre-mitigation value. The line integrated density is converted into a line average density using the interferometer path length. The number of injected impurities is calculated from the change in the pressure of the injection volume during mitigation. Some previous studies of the fuelling efficiency on ASDEX-Upgrade and Tore Supra [15, 13] have made the simplification that the impurities are singly ionized. In this work, for simplicity, the assumption of $Z = 1$ is also applied with the understanding that this will give an upper bound for the fuelling efficiency and it is more likely that $Z \approx 2\text{--}3$ for argon and neon during the current quench. Other tokamaks [8, 10] use a current decay model to estimate the current quench plasma temperature and determine the ionisation state of the injected impurities. The current quench model is not applied on MAST as the absence of a close fitting vessel wall makes the vessel inductance and wall time difficult to estimate, which is likely to introduce a significant error in the derived values.

The fuelling efficiency (figure 16) is determined by the number of impurities delivered to the plasma edge prior to the

start of the current quench phase. The fuelling efficiency is the highest for helium, as the propagation speed is the highest for this species. Increasing the impurity mass leads to a slowing of the propagation time and a decrease in the fuelling efficiency, as seen from the neon and argon traces. The Ar/He mixture behaves in a manner similar to helium, suggesting that the addition of the argon does not hinder the assimilation into the plasma. Increasing the injection quantity leads to a reduction in the fuelling efficiency. ASDEX-Upgrade results [15] show a fuelling efficiency of the order 30% for neon and helium at similar injected quantities to those used on MAST. The ASDEX-Upgrade fuelling efficiencies are similar to those seen in Tore Supra [13], which uses a time dependent method, where fuelling efficiencies are in the range 20–30%. The fuelling efficiency for a given plasma will be limited by the number of particles which are able to interact with the bulk plasma. The design of MAST with a large vacuum vessel volume (50 m³) compared to the plasma volume (10 m³) allows a region into which the gas can expand without interaction with the plasma which limits the interaction of the injected impurities with the plasma. The limited interaction between the impurities and the plasma in MAST could explain the low fuelling efficiencies seen in comparison to results from ASDEX-Upgrade and Tore Supra. The fall in fuelling efficiency, and the limit to the reduction in divertor power loading with increasing injection quantity (figure 9), could also be explained by the injected impurities filling the region between the plasma and the vacuum vessel instead of interacting with the plasma.

7. Current quench phase

The rapid cooling of the plasma during the thermal quench phase increases the plasma resistance, leading to the current quench phase. The increased resistance leads to the conversion of the magnetic energy, stored via the plasma current, into thermal energy through ohmic heating of the cooled plasma [4]. The thermal energy is then lost from the plasma either via radiation or by deposition onto the divertor. The current quench can generate three phenomena. The rapid decay of the current quench can generate induced currents (also known as eddy currents) in the vacuum vessel. The size of the induced currents will depend on the duration of the current decay relative to the penetration time into the vacuum vessel or support structures [1]. The induced currents can generate forces on the vacuum vessel or support structures through their interaction with the toroidal or poloidal magnetic fields. In addition, the vertical displacement of the plasma during the current quench can bring the plasma into contact with the vessel wall. The contact between the plasma and the vessel allows current from the plasma to flow in the vessel walls. The current which flows is known as a halo current and the poloidal component of the halo current can interact with the toroidal field to generate structural stresses on the vessel. The final effect of the current quench is to generate a large toroidal electric field as the plasma current decays away. The large electric field can lead to the acceleration of electrons in the plasma to relativistic velocities which are known as runaway electrons. The interaction of the runaway electrons with material surfaces gives localized

heating and melting of the surfaces [5]. Mitigation of these runaway electrons requires the injection of a sufficient amount of gas to collisionally suppress the runaways [1].

The effect of mitigation on the current quench is to speed up the current quench time by increasing the post thermal quench plasma resistivity. The increased speed of the current quench leads to a lower plasma current if the plasma undergoes a VDE. As a result of the lower plasma current during the interaction of the plasma with the vessel, the halo current fraction can be reduced.

7.1. Current quench times

The effect of MGI on the current quench time can be assessed by measuring the decay time of the current as a function injected quantity. The typical measure of the current quench time is determined from the time taken for the plasma current to decay from 80% to 20% of the pre-current quench value, normalized to the poloidal area of the plasma [1]. The mitigated discharges plotted in figure 17 undergo a loss of vertical control during the current quench, which is also seen in unmitigated disruptions. The loss of vertical control leads to the plasma interacting with the upper divertor and occurs later in the mitigated discharges. The toroidal component of the halo current generated by the interaction of the plasma with the vessel can contribute to the plasma current measurement, as the plasma current Rogowski encompasses the coil supports and divertor structures in which the halo current is likely to flow. The mitigation of the discharges moves the onset of the VDE into the 80–20% decay of the plasma current, which prevents an accurate measure of the current decay from being made from the 80% to 20% decay in mitigated disruptions. The period of the current quench where the current falls from 100% to 80% is unaffected by the additional current from the toroidal component of the halo current, and for this reason the normalized current decay time is derived from the decay of the plasma current from 100% to 80%. Previous studies [8] of the current quench time have used the 100–70% time to determine the current quench time instead of the 80–20% time due to the presence of runaway electrons. The decay time, t_{100-80} is plotted in figure 17 for a range of different injection quantities using Ar(10%)/He mitigation. The fit to the t_{100-80} decay suggests that saturation of the current quench time will occur as the injected quantity is raised further.

The mitigation of runaway electrons in ITER requires a significant increase in the injected quantity over that required for the mitigation of heat loads [1]. The large quantity of gas required is partly due to the density which must be attained in ITER to collisionally suppress the runaways, but also due to the low fuelling efficiency expected in ITER, based on the results from existing devices [15]. One consequence of increased injection quantity is that the current quench time shortens. The shortening of the current quench time produces larger induced currents in the vessel [9]. The limit placed on the current quench time on ITER by the stresses generated by induced currents is 1.67 ms m^{-2} [36]. A concern for MGI is that to mitigate the runaways, the increased level of injection will lead to induced currents which exceed the ITER limit. It is clear

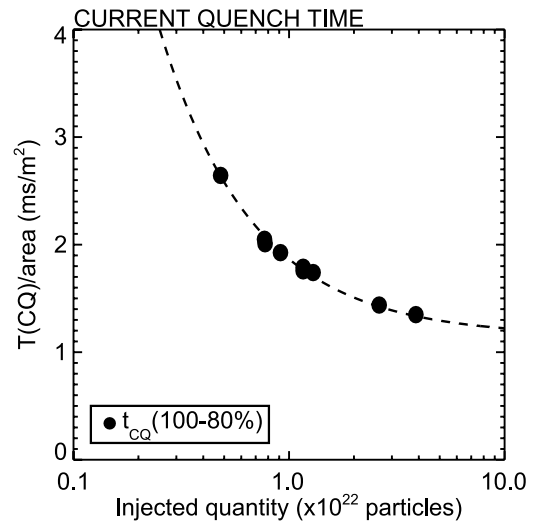


Figure 17. Current quench time for 100% decay, the 100% to 80% decay of the plasma current and normalized to the poloidal cross sectional area. The data shown use injection of varying quantities of an argon (10%) helium mixture. The mitigated plasma is an ohmic double null plasma.

from figure 17 that the current quench rate appears to saturate with increasing injection quantity, which confirms results from JET [8] and ASDEX-Upgrade [15]. The observation of current quench time saturation is promising for disruption mitigation in ITER, as sufficient impurities can be injected into the vessel to provide for runaway electron suppression but the effect on the current quench rate will be unaffected by this increased injection quantity.

The MAST data show that the current quench time saturates at $1\text{--}1.3 \text{ ms m}^{-2}$ in mitigated disruptions, which is below the ITER limit. The current quench time scales in unmitigated disruptions in MAST are similar to the mitigated disruptions with a quench time of between 1.6 and 2.0 ms m^{-2} . The rapid current quench in MAST is supported by NSTX results, suggesting that this is a feature of spherical tokamaks [37].

Measurements of the current quench time in LSN plasmas show that the quench time is unaffected by injected quantity or species. The current quench time in LSN mitigated plasmas is 1.0 ms m^{-2} , which is also the duration of the current quench in unmitigated LSN discharges. LSN plasmas are more vertically unstable than double null plasmas [1] and in MAST discharges undergo a VDE earlier in the current quench phase. A possible explanation for the constant quench time in LSN discharges is that the current decay is controlled by the loss of vertical control quenching the plasma within the vessel structure, rather than a resistive decay of the current in a cold, post thermal quench plasma.

7.2. Halo currents

The halo currents generated during a disruption are monitored in MAST using a series of Rogowski coils located around the vessel [38]. The halo currents can be monitored in two ways. Firstly, the magnitude of the halo current can be measured, which is normalized to the plasma current prior to

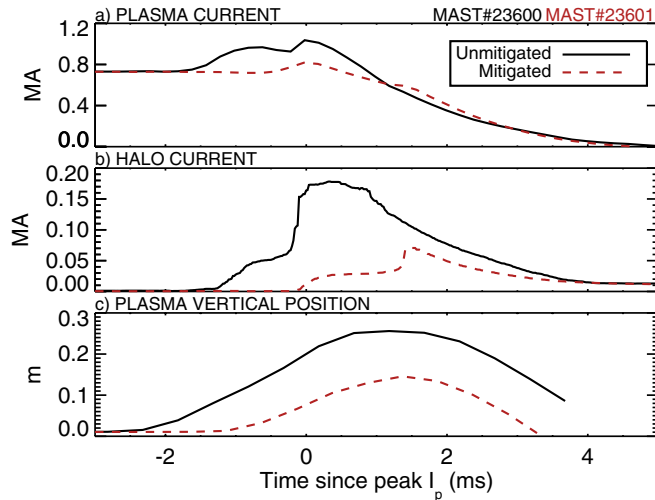


Figure 18. The measured maximum halo current during the disruption is plotted as a function of time after the thermal quench. (a) shows the plasma current during the current quench and (b) shows the peak halo current measured during the disruption. The vertical position of the plasma is shown in (c). The normalized current quench time (80–20%) for the unmitigated case is 2.07 ms m^{-2} , and 1.76 ms m^{-2} in the mitigated case.

the mitigation. Secondly, the asymmetry of the halo currents toroidally can be measured using the toroidal peaking factor (TPF) [1]. The analysis of mitigated disruptions in terms of the peak halo current and the TPF presented here follows that previously used on MAST [39].

The effect of mitigation on halo current formation can be assessed by comparing the halo currents generated in an unmitigated disruption to those of a mitigated disruption. The halo current generated in a mitigated disruption is shown in figure 18(b) along with the halo current in a matching unmitigated disruption. The halo current measured during the disruption is shown as a function of time after the thermal quench, for the mitigated case (dashed red line) and the unmitigated case (solid black line).

A clear reduction in the halo duration and magnitude can be seen from figure 18, with the peak halo current falling by 44% with mitigation and the duration of the halo current decreasing from 6 ms in the unmitigated case to 5 ms in the mitigated case. The rise in the halo current as a result of the VDE can be seen in both cases, with the peak halo current occurring 1.75 ms after the thermal quench in the unmitigated case and 2.5 ms after the thermal quench in the mitigated case. The sudden rise in the halo current at these times is consistent with the plasma vertical position, as seen in figure 18(c). The plasma position at 1.75 ms after the thermal quench in the mitigated case is approximately 0.15 m, this displacement is also seen at time of the peak halo current in the mitigated case. The motion of the plasma will lead to contact between the plasma and the coils inside the vacuum vessel. High speed imaging of the plasma shows that the time of the peak halo current is correlated with the interaction of the plasma with the P3 poloidal field coil in MAST, which is consistent with the description above.

The early VDE seen in the unmitigated disruption occurs at a plasma current of 900 kA compared to the mitigated case,

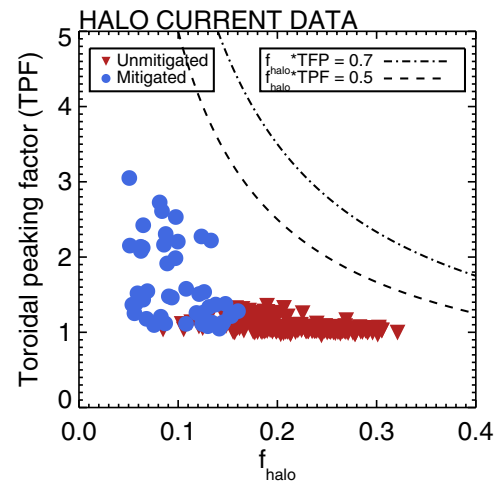


Figure 19. The TPF during the disruption as a function of the halo current fraction, f_{halo} , for mitigated (blue circles) and unmitigated disruptions (red triangles).

when the plasma current is approximately 600 kA. The lower plasma current in the mitigated case at the onset of the VDE leads to the lower halo currents seen during mitigation.

The TPF and halo current fraction, $f_{\text{halo}} = I_{\text{halo}}^{\text{MAX}}/I_p^{\text{disruption}}$ can be determined for mitigated discharges and unmitigated discharges. A fault with the halo current detectors limits the data which is available to discharges with Ar/He injection only. To enable the reduction in the halo current to be quantified, the mitigated data can be compared to a database of unmitigated disruptions, which is shown in figure 19. The forces generated by halo currents arise from toroidal asymmetries in the halo currents. Therefore, the product of the TPF with the halo fraction is indicative of the structural stress likely to be generated during the disruption.

It is clear from figure 19 that mitigation decreases the halo current fraction, whilst increasing the TPF. The reduction in the halo current fraction arises as a result of the decreased current quench time. The fast current quench time decreases the peak plasma current at the time of interaction with the vessel and allows less time for the VDE to occur. However, it should be noted that the mitigated disruptions, and the unmitigated disruptions, in MAST are within the $\text{TPF} \times f_{\text{halo}} \leq 0.75$ limit imposed by the ITER design [1].

8. Summary

The mitigation of disruptions using MGI is a key area of research for next step devices, such as ITER. Investigation of disruption mitigation on MAST has shown that MGI is an effective means of mitigating the heat loads and structural stresses generated during a disruption.

The injection of a range of gas species of differing masses, atomic charge and a range of injected quantities, corresponding to between 10 and 150 times the plasma inventory, has allowed the study of several features of disruption mitigation via MGI. The response time of a disruption mitigation system is determined by the time between the triggering of the valve and the arrival of the impurities at the plasma edge. Measurements

of the arrival of the gas at the plasma using high speed imaging has shown that the propagation of the impurities occurs at between 1.55 and 2.1 times the sound speed of the impurities.

The arrival of the impurities at the plasma edge give rise to line radiation, which acts to cool the plasma. The cooling time can be defined as the time between the arrival of the gas and the end of the thermal quench (determined by the peak in the current spike). The cooling time is the longest for helium injection, with heavier impurities showing faster cooling times. Increasing injection quantity gives rise to faster cooling, most likely as a result of the increased number of radiating impurities. During the cooling phase the impurities mix into the plasma edge, measurements of the electron density rise during this phase shows that helium gives the largest density rise. The largest rise for helium can be explained as it has the longest cooling time and the fastest sound speed, therefore, more helium atoms can mix with the plasma during the cooling phase than the heavier species, such as argon. These observations are also supported by measurement of the fuelling efficiency which is the highest for helium.

The radiation of the energy stored in the plasma during the cooling phase decreases the heat loads to the divertor during the thermal quench phase. Measurements of the divertor energy loads during a mitigated disruption show that the peak energy load falls by 60% compared with an unmitigated disruption. The decrease in peak power load is accompanied with a decrease in the total energy load to the divertor, with mitigated disruptions showing divertor energy loads of 40% of the total stored energy. Unmitigated disruptions by contrast show divertor energy loads of 80% of the total stored energy. A corresponding rise in radiated power is observed during mitigation to account for the decrease in the divertor loads. Analysis of the background emission during mitigation has shown that there is a limited effect on the infrared measurements of the power to the divertor, with the background level corresponding to 7% of the total signal in the worst case, but this is within the error of the IR system as a result of surface layers or toroidal asymmetries.

The generation of runaway electrons during disruptions is major concern for ITER. Although runaway electrons are not generated on MAST, due to the low toroidal magnetic field (0.5 T), the high levels of injected impurities required for runaway electron suppression can affect the speed of the current quench. Increased injection quantity has been seen to increase the rate at which the current quench occurs, which leads to larger induced currents during the disruption. The current quench time in MAST has been seen to saturate with increased injection quantity, which confirms the results from other conventional aspect ratio tokamaks.

Acknowledgments

The disruption mitigation valve used in these studies was supplied via collaboration with Forschungszentrum Jülich. This work was part funded by the RCUK Energy Programme under grant EP/I501045 and the European Communities under

the Contract of Association between EURATOM and CCFE. The views and opinions expressed herein do not necessarily reflect those of the European Commission. The authors would also like to thank Dr. Sergei Gerasimov for helpful comments and for proof reading the manuscript.

© Euratom 2012.

References

- [1] Hender T C *et al* 2007 Progress in the ITER physics basis chapter 3: MHD stability, operational limits and disruptions *Nucl. Fusion* **47** S128–202
- [2] Schüller F C 1995 Disruptions in tokamaks *Plasma Phys. Control. Fusion* **37** A135–62
- [3] Federici G 2006 Plasma wall interactions in ITER *Phys. Scr.* **T124** 1–8
- [4] Granetz R *et al* 2007 Gas jet disruption mitigation studies on Alcator C-Mod and DIII-D *Nucl. Fusion* **47** 1086–91
- [5] Lipa M *et al* 2003 Effects of supra-thermal particle impacts on Tore Supra plasma facing components *Fusion Eng. Des.* **66–68** 365–9
- [6] Yoshino R *et al* 1997 Fast plasma shutdown by killer pellet injection in JT-60U with reduced heat flux on the divertor plate and avoiding runaway electron generation *Plasma Phys. Control. Fusion* **39** 313
- [7] Taylor P L *et al* 1999 Disruption mitigation studies in DIII-D *Phys. Plasmas* **6** 1872–79
- [8] Lehnen M *et al* 2011 Disruption mitigation via massive gas injection in JET *Nucl. Fusion* **51** 123010
- [9] Pautasso G *et al* 2007 Plasma shut-down with fast impurity gas puff on ASDEX-Upgrade *Nucl. Fusion* **47** 900–13
- [10] Bozhnekov S A *et al* 2008 Generation and suppression of runaway electrons in disruption mitigation experiments in TEXTOR *Plasma Phys. Control. Fusion* **50** 105007
- [11] Whyte D G *et al* 2003 Disruption mitigation with high pressure noble gas injection *J. Nucl. Mater.* **313–316** 1239–46
- [12] Granetz R *et al* 2006 Gas jet disruption mitigation studies on Alcator C-Mod *Nucl. Fusion* **46** 1001–8
- [13] Reux C *et al* 2010 Experimental study of disruption mitigation using massive gas injection of noble gases on Tore Supra *Nucl. Fusion* **50** 095006
- [14] Hollmann E M *et al* 2007 Observation of q -profile dependence in noble gas injection radiative shutdown times in DIII-D *Phys. Plasmas* **14** 012502
- [15] Pautasso G *et al* 2009 Disruption studies in ASDEX Upgrade in view of ITER *Plasma Phys. Control. Fusion* **51** 124065
- [16] Thornton A J *et al* 2012 Plasma profile evolution during disruption mitigation via massive gas injection on MAST *Nucl. Fusion* **52** 063018
- [17] Hollmann E M *et al* 2008 Measurements of injected impurity assimilation during massive gas injection experiments in DIII-D *Nucl. Fusion* **48** 115007
- [18] Lloyd B *et al* 2011 Overview of physics results from MAST *Nucl. Fusion* **51** 094013
- [19] Bozhnekov S A *et al* 2007 Main characteristics of the fast disruption mitigation valve *Rev. Sci. Instrum.* **78** 033503
- [20] Hollmann E M *et al* 2005 Measurements of impurity and heat during noble gas jet initiated fast plasma shutdown for disruption mitigation in DIII-D *Nucl. Fusion* **45** 1046–55
- [21] Thornton A J *et al* 2011 Disruption mitigation on MAST *J. Nucl. Mater.* **415** S836–40
- [22] Landau L D and Lifshitz E M 1987 *Fluid Mechanics* 2nd edn (Oxford: Butterworth-Heinemann)

- [23] Savtchikov A *et al* 2002 Development of a fast valve for mitigating disruptions in tokamaks *Rev. Sci. Instrum.* **73** 3490–93
- [24] Finken K H *et al* 2011 A new disruption mitigation valve and gas flow in guiding tubes of different diameter *Nucl. Fusion* **51** 033007
- [25] Kruezi U *et al* 2009 Massive gas injection experiments at JET: Performance and characterisation of the disruption mitigation valve *36th EPS Conf. on Plasma Physics (Sofia, Bulgaria)*
- [26] De Temmermann G *et al* 2010 Thermographic studies of heat load asymmetries during MAST L-mode discharges *Plasma Phys. Control. Fusion* **52** 095005
- [27] Herrmann A *et al* 1995 Energy to the ASDEX-Upgrade divertor plates determined by thermography and calorimetry *Plasma Phys. Control. Fusion* **37** 17–29
- [28] Herrmann A *et al* 2001 Limitations for divertor heat flux calculations of fast events in tokamaks *27th Conf. on Plasma Physics and Controlled Fusion (Madeira, Portugal)*
- [29] Delchambre E *et al* 2009 Effect of micrometric hot spots on surface temperature measurement and flux calculation in the middle and long infrared *Plasma Phys. Control. Fusion* **51** 055012
- [30] Cox M 1999 The Mega Amp Spherical Tokamak *Fusion Eng. Des.* **46** 397–404
- [31] Loarer Th *et al* 2007 Surface temperature measurements by means of pulsed photothermal effect in fusion devices *J. Nucl. Mater.* **363–365** 1450
- [32] Kirk A *et al* 2004 ELM characteristics in MAST *Plasma Phys. Control. Fusion* **46** 551–72
- [33] Finken K H *et al* 2008 Gas flow analysis of a disruption mitigation valve *Nucl. Fusion* **48** 115001
- [34] Lao L L *et al* 1985 Reconstruction of current profile parameters and plasma shapes in tokamaks *Nucl. Fusion* **25** 1611
- [35] Tournianski M *et al* 2005 Anisotropic fast neutral particle spectra in the MAST spherical tokamak *Plasma Phys. Control. Fusion* **47** 671–84
- [36] Wesley J *et al* 2006 Disruption characterization and database activities for ITER *Proc. 21st Int. Conf. on Fusion Energy Research (Chengdu, China)* (Vienna: IAEA) CDROM IT/P1-21
- [37] Gerhardt S P *et al* 2009 Characterization of the plasma current quench during disruptions in the National Spherical Torus Experiment *Nucl. Fusion* **49** 025005
- [38] Edlington T *et al* 2001 MAST magnetic diagnostics *Rev. Sci. Instrum.* **72** 421–5
- [39] Counsell G F *et al* 2007 On the magnitude and distribution of halo currents during disruptions on MAST *Plasma Phys. Control. Fusion* **49** 435–46